Journal of Volcanology and Geothermal Research 325 (2016) 1–14

Contents lists available at ScienceDirect

Journal of Volcanology and Geothermal Research

journal homepage: www.elsevier.com/locate/jvolgeores

Great Balls of Fire: A probabilistic approach to quantify the hazard related to ballistics — A case study at La Fossa volcano, Vulcano Island, Italy

Sébastien Biass [a,b,*], Jean-Luc Falcone [c], Costanza Bonadonna [a], Federico Di Traglia [d], Marco Pistolesi [d], Mauro Rosi [e], Pierino Lestuzzi [f]

[a] Département des Sciences de la Terre, Université de Genève, 13, Rue des Maraîchers, CH-1205 Genève, Switzerland
[b] Department of Geology and Geophysics, University of Hawaii at Manoa, 1680 East-West Road, Honolulu, HI 96822, USA
[c] Centre Universitaire dInformatique, Université de Genève, Batelle - Batiment A, 7, route de Drize, CH-1227 Carouge, Switzerland
[d] Dipartimento di Scienze della Terra, Università degli Studi di Firenze, Via La Pira 4, 50121, Firenze, Italy
[e] Dipartimento di Scienze della Terra, Università di Pisa, Via Santa Maria 53, 56126, Pisa, Italy
[f] Ecole Polytechnique Fédérale de Lausanne, ENAC IIC IMAC, GC G1 557, Station 18, CH-1015 Lausanne, Switzerland

ARTICLE INFO

Article history:
Received 7 December 2015
Received in revised form 9 June 2016
Accepted 13 June 2016
Available online 17 June 2016

Keywords:
Probabilistic hazard assessment
Volcanic ballistic projectiles
Pre-event impact assessment
Physical vulnerability
Vulcano Island La Fossa

ABSTRACT

We present a probabilistic approach to quantify the hazard posed by volcanic ballistic projectiles (VBP) and their potential impact on the built environment. A model named *Great Balls of Fire* (GBF) is introduced to describe ballistic trajectories of VBPs accounting for a variable drag coefficient and topography. It relies on input parameters easily identifiable in the field and is designed to model large numbers of VBPs stochastically. Associated functions come with the GBF code to post-process model outputs into a comprehensive probabilistic hazard assessment for VBP impacts. Outcomes include probability maps to exceed given thresholds of kinetic energies at impact, hazard curves and probabilistic isoenergy maps. Probabilities are calculated either on equally-sized pixels or zones of interest.

The approach is calibrated, validated and applied to La Fossa volcano, Vulcano Island (Italy). We constructed a generic eruption scenario based on stratigraphic studies and numerical inversions of the 1888–1890 long-lasting Vulcanian cycle of La Fossa. Results suggest a $\sim 10^{-2}$% probability of occurrence of VBP impacts with kinetic energies $\leq 10^4$ J at the touristic locality of Porto. In parallel, the vulnerability to roof perforation was estimated by combining field observations and published literature, allowing for a first estimate of the potential impact of VBPs during future Vulcanian eruptions. Results indicate a high physical vulnerability to the VBP hazard, and, consequently, half of the building stock having a $\geq 2.5 \times 10^{-3}$% probability of roof perforation.

1. Introduction

Volcanic ballistic projectiles (VBP) decouple from the jet phase of explosive events to follow a near-ballistic trajectory modified by drag forces (Alatorre-Ibargüengoitia et al., 2012). VBPs can be distinguished between blocks, typically of angular shape and lithic origin, and bombs, typically of rounded shape and juvenile origin. These ballistic projectiles can be produced in all types of volcanic eruptions, but are particularly abundant with Vulcanian, Strombolian and phreatic styles (e.g. Feeley and Winer, 2009; Vanderkluysen et al., 2012; Kaneko et al., 2016). VBPs constitute a major threat in proximal areas (i.e. a few kilometres from the vent) due to their high kinematic energies and temperatures that can impact life and the built environment and ignite fires. As examples, Pomonis et al. (1999) reported VBPs <1 kg penetrating thatched and galvanized iron roofs during previous eruptions of Furnas volcano (Azores), and Pistolesi et al. (2011), and Rosi et al. (2013) reported wildfires triggered by incandescent blocks during the 2007 crisis of Stromboli.

Numerous models for ballistic ejection have been developed since the 1940's, primarily to invert field observations and estimate eruptive conditions (e.g. ejection velocity; Minakami, 1942; Fudali and Melson, 1971; Wilson, 1972; Steinberg and Lorenz, 1983). Although accounting for drag effects, initial models considered the ejection of blocks into a still atmosphere, commonly leading to an overestimation of drag forces and, consequently, unrealistically high ejection velocities. In the context of Vulcanian eruptions, later models introduced a caprock accelerated by the gas expansion and behaving as a coherent plug until a maximum velocity is reached, at which point the fractured caprock disaggregates and individual ballistic blocks are released (Self et al., 1979; Wilson, 1980; Fagents and Wilson, 1993). This disaggregation height has been

* Corresponding author at: Department of Geology and Geophysics, University of Hawaii at Manoa, 1680 East-West Road, Honolulu, HI 96822, USA.
E-mail address: sbiasse@hawaii.edu (S. Biass).

http://dx.doi.org/10.1016/j.jvolgeores.2016.06.006
0377-0273/

recently suggested to occur when the acceleration is 8% of the initial acceleration of the caprock (Alatorre-Ibargüengoitia et al., 2012). This implies a region of reduced drag in the vicinity of the eruptive source, within which the surrounding air moves radially from the source at a velocity comparable to that of the clasts (Fagents and Wilson, 1993). Using this concept, the effect of drag becomes important only when the velocity of the clast gradually decouples from that of the surrounding air, which allows to reproduce observed deposits with significantly lower ejection velocities.

Amongst all models, *Eject*! (Mastin, 2001) accounts for a region of reduced drag (defined as a radius above the vent) and a variable drag coefficient and to describe the ballistic motion as a function of input parameters (e.g. block density, ejection velocity and angle). De' Michieli Vitturi et al. (2010) proposed a coupled Eulerian–Lagrangian model to describe the dynamics of large particles during Vulcanian eruptions, providing a detailed parametrization of the complex radial and vertical acceleration and deceleration patterns of the initial jet phase. Alatorre-Ibargüengoitia et al. (2012) presented a model coupling lab measurements of the effect of shape on the drag of volcanic particles and a caprock model relating the energy consumption required by fragmentation to the ejection velocity of ballistics (Alatorre-Ibargüengoitia and Delgado-Granados, 2006; Alatorre-Ibargüengoitia et al., 2010). Recently, Tsunematsu et al. (2014) developed a new approach accounting for multiple particles and collision between bombs.

The main aim of hazard assessments is to quantify the geographical and temporal probabilities of occurrence of a hazardous phenomenon of a given magnitude (Fournier d'Albe, 1979; Mendoza-Rosas and De la Cruz-Reyna, 2008). In volcanology, where eruptions constitute a multi-hazard system, this process is commonly achieved by i) the field characterization of the deposits in order to constrain and quantify eruption source parameters (ESPs), ii) the compilation of a catalogue of eruptions and phenomena at a given volcano to infer eruption scenarios and iii) the forward modelling of a given phenomenon using appropriate models (e.g. Cioni et al., 2003; Biass et al., 2014). Recent hazard assessments in all fields of natural hazards increasingly rely upon probabilistic techniques in order to account for the inherent uncertainty of natural processes (e.g. Geist and Parsons, 2006; Gonzalez et al., 2009; Heneka and Hofherr, 2011). In volcanology, stochastic strategies have been widely applied to the modelling of tephra (e.g. Bonadonna, 2006; Jenkins et al., 2012) and, more recently, lava flows (e.g. Connor et al., 2012), for which probabilistic eruption scenarios are characterized by relevant ESPs defined as probability distributions. Hazard assessments for ballistics are, however, often based on a deterministic definition of eruption scenarios aiming at producing hazard zones for different block size, ejection angle and initial velocities (Alatorre-Ibargüengoitia et al., 2006; Alatorre-Ibargüengoitia et al., 2012; Sandri et al., 2014). Recently, Fitzgerald et al. (2014) proposed a new probabilistic approach based on the model of Tsunematsu et al. (2014), in which crucial ESPs were quantified in terms of mean value and standard deviation from the study of 3587 impact craters.

We propose a new approach to assess the hazard and the impact on the built environment related to the ejection of ballistic blocks, compiled in a package called *Great Balls of Fire* (GBF; Lewis, 1957, Sun. Studio). The first part of the GBF package comprises a model written in Scala, with the main features being i) the stochastic sampling of ESPs, ii) the implementation of a variable drag coefficient, iii) the ability to use a DEM to account for topographic barriers and iv) the possibility to work on a single CPU or on a cluster of computers. The second part of the package provides *Matlab* routines to post-process model outputs into probabilities of VBP impacts to exceed energy thresholds, exporting results in a shape readable by most GIS platforms. This paper first describes the ballistic model, which is then tested and validated using field measurements of VBPs produced during the last Vulcanian eruption of La Fossa Volcano, Vulcano Island, Italy. We then constructed an eruption scenario for a Vulcanian eruptive style and applied the method to compile probabilistic hazard maps for the ejection of VBPs at La Fossa. Outcomes are combined with a rapid assessment of the built environment to produce a first–order pre–event impact assessment of the buildings stock.

2. Case study of Vulcano Island

Vulcano is the southernmost island of the Aeolian archipelago and, along with Lipari and Stromboli, one of the active volcanic systems of the archipelago (De Astis et al., 1997; Gioncada et al., 2003, Fig. 1). The sub-aerial activity of Vulcano started between 135 and 120 ka (Zanella et al., 2001), after which volcanism migrated N-NW, generating a composite structure of four, juxtaposed volcanic edifices including the cone of La Fossa, center of the current activity. The eruptive history and structure of the 391 m-high La Fossa cone has been studied by (Keller, 1980; Frazzetta et al., 1983; Frazzetta et al., 1984; Gioncada et al., 2003; Arrighi et al., 2006; Dellino et al., 2011; De Astis et al., 2013; Di Traglia et al., 2013).

The eruptive history of the last 1000 years was reconstructed based on stratigraphic studies (Di Traglia, 2011; De Astis et al., 2013) and historical chronicles (Mercalli and Silvestri, 1891; De Fiore, 1922). Following the nomenclature of Di Traglia et al. (2013), the most recent deposits were grouped in two stratigraphic clusters including the Palizzi–Commenda Eruptive Cluster (PCEC) and the Gran Cratere Eruptive Cluster (GCEC).

The PCEC is divided in the Palizzi and the Commenda units (Frazzetta et al., 1983; Frazzetta et al., 1984; Dellino and La Volpe, 1997; Di Traglia, 2011; Dellino et al., 2011; De Astis et al., 2013). The Palizzi unit is a semi–persistant eruptions characterized by shifts between explosive and effusive styles, for which no VBP is identified in the stratigraphy. The Commenda unit is a magmatic–hydrothermal eruption (Gurioli et al., 2012) that produced the Breccia di Commenda deposit (~1240 CE), characterized by a high lithic–to–juvenile ratio and dense lithic VBPs (Gurioli et al., 2012; Di Traglia et al., 2013).

The GCEC (1440 CE–1890 CE; Di Traglia et al., 2013) started with a steam-blast eruption on the 5th of February 1444 (Mercalli and Silvestri, 1891). Around 1550 CE occurred the first of the eight Vulcanian eruptions of the GCEC (Di Traglia et al., 2013). The last eruption occurred in 1888–1890 and was characterized by plume heights between 1 and 10 km and an intense ejection of VBPs. Different morphologies were produced at various stages of the eruption, with dense lithic blocks occurring at the beginning and the end of the cycle and juvenile breadcrust bombs ejected mostly halfway through the eruption (Bianchi, 2007; Di Traglia, 2011). Outcrops with VBPs associated with the 1888–1890 eruption are shown in Fig. 1 (S1–S3). In addition, historical reports also mention that a warehouse located close to the so-called Stevenson Castle (pink star on Fig. 1) was impacted by a VBP.

About 800 people permanently live on Vulcano, but daily peaks can reach 20,000 during the summer season. Four settlements are present on the island. In the south, Piano lies on top of the filled caldera of Vulcano Primordiale and is the home of most of the permanent inhabitants. The remaining settlements of the Porto area, Vulcanello and Lentia, comprise most of the hotels and tourism facilities. The topography (Fig. 1) suggests that Piano and Lentia are sheltered by barriers, whereas the Porto and Vulcanello areas lie on a plain directly North of the La Fossa cone.

3. The GBF model

The GBF model is based on classical movement equations using gravity and drag force and accounts for a standard atmosphere, the influence of the wind and a region of reduced drag following Mastin (2001). The simulator was implemented using the Scala language and parallelized with the Akka actor framework. User interactions are provided through a minimalist command line interface and all simulation settings are defined in a simple configuration file.

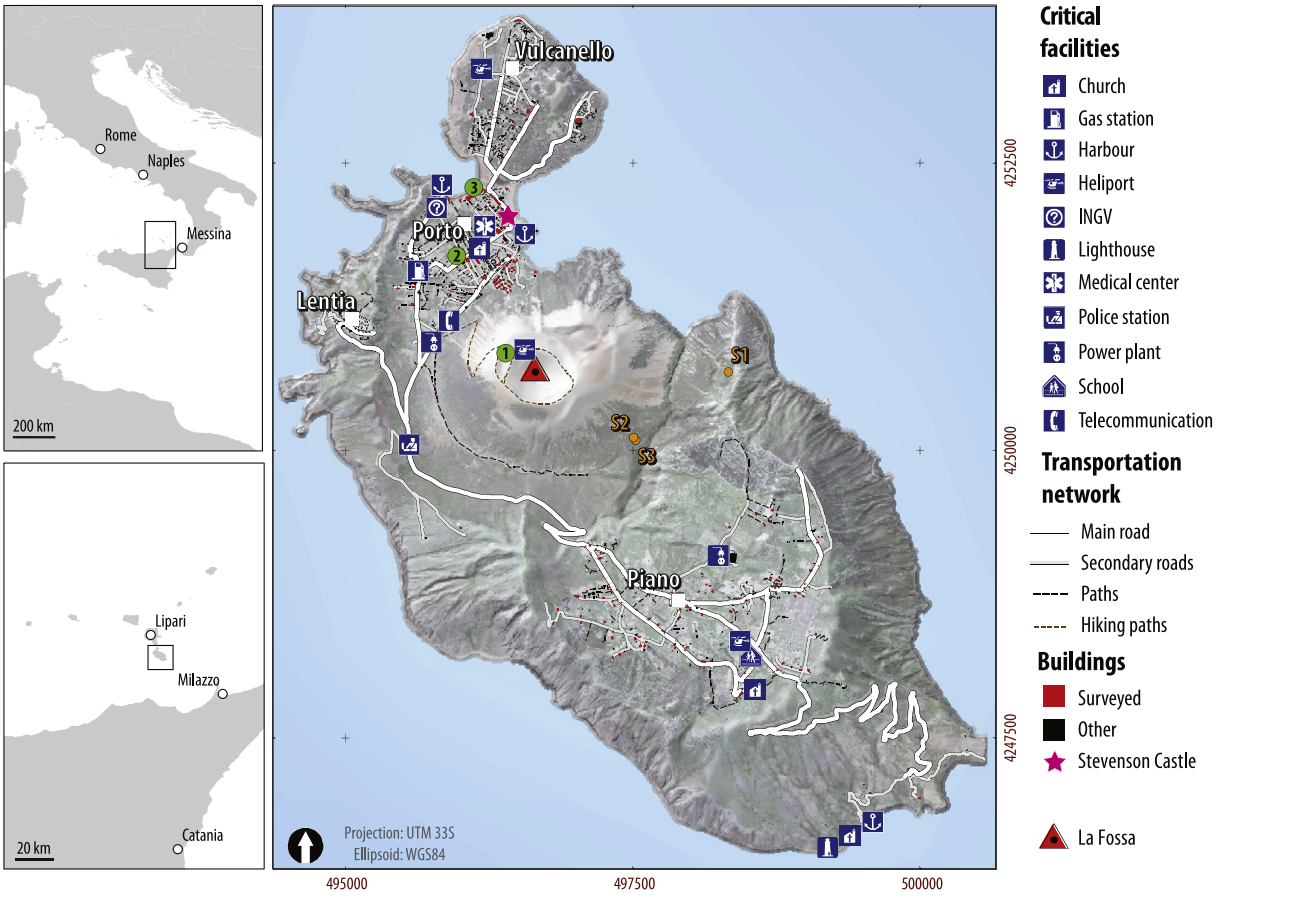

Fig. 1. Overview of Vulcano Island, showing the main localities used throughout the text (white squares), the road network, the location of critical infrastructures and buildings footprints. Green dots show the reference points used for the sensitivity analysis. Orange dots show the field location of the sampling sites.
Adapted from Biass et al. (2016).

3.1. Governing equations

Each particle is approximated by a sphere and described by a mass m, an average diameter D, a position $\mathbf{r}$ and a velocity $\mathbf{v}$. The VBP trajectory is described by the following equations:

$$\mathbf{u} = \mathbf{v} - \mathbf{w} \tag{1}$$

$$\ddot{\mathbf{r}} = \dot{\mathbf{v}} = \mathbf{a} = \frac{-\rho_a A C_d \mathbf{u}|\mathbf{u}|}{2m} + \mathbf{g} \tag{2}$$

where A is the fluid cross area, C_d the drag coefficient, ρ_a the air density, $\mathbf{u}$ the velocity of the VBP relative to the wind $\mathbf{w}$ and $\mathbf{g}$ the acceleration gravity vector. The computation of the drag coefficient and the air density depends on the VBP altitude and velocity. For a given altitude z, the air temperature T and pressure p are computed using the following formulas:

$$T(z) = T_0 + \gamma z \tag{3}$$

$$p(z) = p_0 \left(\frac{T(z)}{T_0}\right)^{-\frac{g}{R\gamma}} \tag{4}$$

where T_0 and p_0 are respectively the air temperature and pressure at sea level, γ is the thermal lapse and R the gas constant. This allows the computation of both the air density and the kinematic viscosity ν_a:

$$\rho_\alpha(z) = \frac{p(z)}{RT(z)} \tag{5}$$

$$\nu_a(z) = \left(\frac{6.70810^{-3}}{T(z) + 117}\right) \cdot \left(\frac{T(z)}{273}\right)^{\frac{3}{2}}. \tag{6}$$

The particle Reynolds number, based on the air characteristics detailed above and the VBP diameter and speed, is used to determine the drag coefficient C_d:

$$Re = \frac{\rho_a u D}{\nu_a} \tag{7}$$

$$C_d = \begin{cases} 0.1 & \text{if } Re > 2 \times 10^{\wedge 5}, \\ 0.5 & \text{else.} \end{cases} \tag{8}$$

Since VBPs are ejected together with an expanding mass of gas, the drag coefficient may be reduced according to the following equation:

$$C_{d\prime} = \begin{cases} C_d \left(\frac{r}{r_d}\right)^2 & \text{ifr} < \text{r}_\text{d}, \\ C_d & \text{else.} \end{cases} \tag{9}$$

3.2. Random VBP generation

The GBF model is implemented with a module for generating VBPs with random initial conditions. Each VBP is generated with ESPs sampled stochastically and constrained either on Gaussian or uniform distributions (Table 1). Each VBP is characterized by a diameter and a

Table 1
Summary of parameters modeled stochastically in the GBF model. $N(\mu,\sigma)$ represents a Gaussian distribution with average μ and standard deviation σ. $U(a,b)$ represents a uniform distribution with values in the interval $[a,b]$.

Parameter	Distribution	Constraint
Ejection velocity (v)	$\in N(v_\mu, v_\sigma)$	$v>0$
Ejection angle (ϕ)	$\in \lvert N(\phi_\mu, \phi_\sigma)\rvert$	
Ejection azimuth (θ)	$\in U(0,2\pi)$	
Density (d)	$\in N(d_\mu, d_\sigma)$	$d>0$
Grain size (Φ)	$\in N(\Phi_\mu, \Phi_\sigma)$	

density, which, assuming a spherical shape, are used to calculate the mass. Additional tests are performed to ensure that all constraints in Table 1 are satisfied, else all parameters are discarded and re-sampled.

3.3. Numerical model and implementation

Eqs. (1)–(9) are solved numerically using Runge–Kutta 4th order with a time step $\Delta t = 0.01$ s. In the absence of an analytic solution, we tested the accuracy of the output by solving the trajectories of 10,000 randomly sampled VBPs with time steps of 0.01 s and 0.001 s. Using the smaller time step as a reference, we computed the absolute error as the distance between impact points under both conditions. The error was <1 m for 99.56% of the VBPs and the maximum recorded error was <3 m. When normalized by the distance between the impact and the vent, only 9 VBPs out of 10,000 had a relative error of >0.01%.

3.4. Validation with field data

The GBF model was validated using the field observation of six VBPs associated with the 1888–1890 eruption presenting sufficient stratigraphic constraints to discard possible reworking and displacement. The VBPs were classified in three typical morphologies including i) lithic blocks, either fresh or altered, ii) thin-rinded breadcrust bombs and iii) thick-rinded breadcrust bombs.

Firstly, the S1 sampling site (Fig. 1; Table 2) comprises one thick–rinded breadcrust bomb identified by Bianchi (2007) characterized by a diameter of 25 cm and a density of 1800 kg m^{-3}, located ~1560 m from the vent. Using the *Eject*!, Bianchi (2007) identified two extreme solutions to reproduce this field observation. On one end, a minimum ejection velocity of 145 m s^{-1} was identified using an ejection angle of 45 ° from vertical. Based on the observations of steep crater slopes during the 1888–1890 eruption (Mercalli and Silvestri, 1891), an inclination of 15 ° from the vertical was used to represent a more realistic ejection angle. Such an angle results in an ejection velocity of 350 m s^{-1}, which is comprised in the higher spectrum of velocities reported in the literature for Vulcanian explosions (e.g. Druitt et al., 2002; Wright et al., 2007; Alatorre-Ibargüengoitia et al., 2012; Maeno et al., 2013). Secondly, the S2 sampling site represents a 20×20 m area where the populations of different VBPs morphologies were studied. From a total of 111 VBPs found in the area, the S2 sampling site shows a dominance of lithic blocks (80%) with minor thin- (14%) and thick-rinded (6%) breadcrust bombs. At the time of the sampling (performed before and for a different purpose than the present paper), the diameter of the most representative VBP of the dominant size population of each morphology was estimated (Table 2). Finally, the S3 sampling site consists of one abnormally large thick-rinded breadcrust bomb Table 2).

We used the GBF model to estimate the ejection velocity and angle reproducing these observations. Sets of simulations of 10^5 particles were performed, varying the ejection velocities between 100 and 350 m·s^{-1} with increment of 25 m·s^{-1}, and angles between 5 and 45 ° from the vertical every 5 °. At each increment, both ejection velocities and angles were allowed a variation characterized by a standard deviation equal to half of the increment. The mean distance calculated over the 10^5 VBPs was calculated for each combination of ejection velocity and angle.

Fig. 2 contours the difference between the mean modelled distance and the observed distance as a function of ejection velocity and ejection angle. The *0 m* line represents the combination of angle and velocity reproducing best the observation, and suggests a continuum of possible solutions. For instance, the altered block in the S2 sampling site can equally be reproduced by sets of angles and velocities of 20 °/120 m·s^{-1} or 10 °/170 m·s^{-1} (turquoise line in Fig. 2). Radiis of reduced drag of 200, 600 and 1000 m are tested (respectively the black, blue and red line in Fig. 2). In general, a set of input parameters falling within the purple region of Fig. 2 suggests an overestimation compared to field observations, whereas the orange region suggests an underestimation.

For the S1 sample, both the GBF and *Eject*! models result in similar minimum conditions, i.e. a velocity of 145 m·s^{-1} for an ejection angle of 45 ° (Fig. 2). In contrast, the GBF model suggests a velocity of ~225 m·s^{-1} for an angle of 15 °, which is significantly lower than the 350 m·s^{-1} suggested by Bianchi (2007) but more realistic when compared to typical ejection velocities reported for Vulcanian explosions (e.g. Druitt et al., 2002; Alatorre-Ibargüengoitia et al., 2006; Wright et al., 2007; Alatorre-Ibargüengoitia et al., 2012; Maeno et al., 2013). Nevertheless, due to the location of the S1 sample (i.e. on the edge of the Piano caldera, 1.6 *km* away from the vent) and the absence of historical report of VBP reaching the Piano caldera, we assume the S1 sample as an extreme case–figure. The S2 and S3 sampling sites are well reproduced by the GBF model (Fig. 2), where an ejection velocity of 150 m·s^{-1} typically requires ejection angles lower than 15–20 °.

Two additional observations can be made from Fig. 2. Firstly, the S2 sampling site shows that for a similar equivalent diameter, thin–rinded breadcrust bombs require higher ejection velocities than thick–rinded breadcrust bombs to reproduce the observations, which is due to the lower kinetic energy of lighter VBPs. Secondly, an increased radius of reduced drag has an overall low influence on the modelled distance, although the effect increases when reproducing impacts farther from the vent (e.g. S1) or for lighter VBPs (thin–rinded breadcrust bomb of S2).

Table 2
Summary of observed VBPs associated with the 1888–1890 eruption used for the field validation of the GBF model. The distance represents the euclidean distance from the actual vent. The sample locations are reported on Fig. 1. *BCB* stands for breadcrust bomb.

Sampling site	Type	Distance (m)	Axis lengths (cm)	Diameter (cm)	Density (kg m^{-3})	
					Mean	Standard dev.
S1	Thick-rinded BCB	1560	–	25	1600	200
S2	Altered block	960	120×65×40	68[a]	2300	100
S2	Fresh block	960	40×35×22	31[a]	2300	100
S2	Thin-rinded BCB	960	47×30×10	24[a]	800	50
S2	Thick-rinded BCB	960	35×30×18	27[a]	1600	200
S3	Thick-rinded BCB	1000	70×50×50	56[a]	1600	200

[a] Equivalent diameter expressed as the geometric mean of the three orthogonal axes.

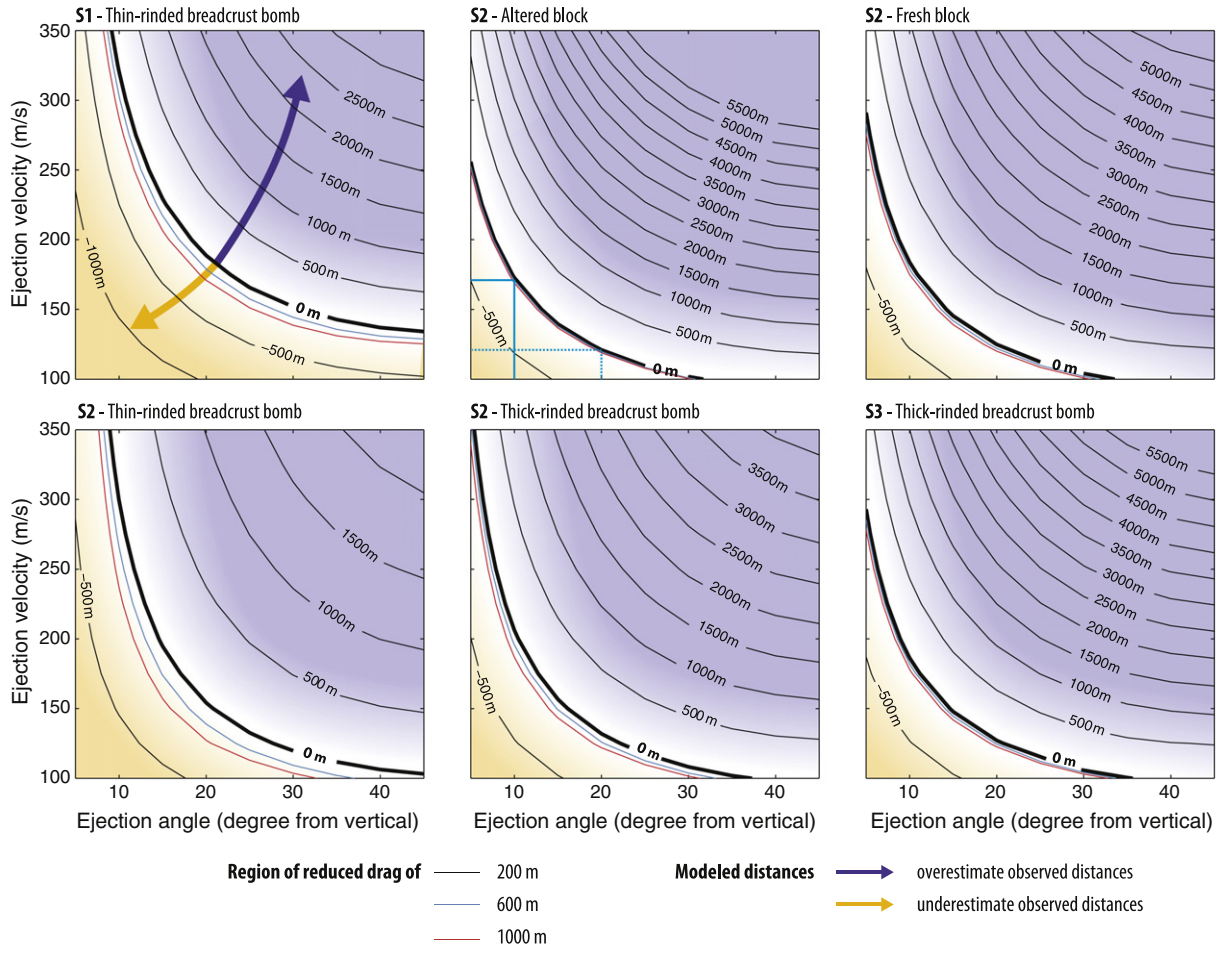

Fig. 2. Difference (in metres) between the mean modelled distance and the observed distance as a function of ejection velocity and ejection angle for all VBP morphologies observed at sampling sites shown in Fig. 1 (orange dots). The white region represents sets of input parameters reproducing best observations. Radii of 200 m (black lines), 600 m (blue line) and 1000 m (red line) are considered.

4. Application to La Fossa Volcano

4.1. Eruptive scenarios

During the activity of the last 1000 years at La Fossa, two main eruptive styles produced VBPs, namely non-juvenile steam blast eruptions (i.e. Commenda unit) and Vulcanian eruptions (Di Traglia et al., 2013; De Astis et al., 2013). Here, we only consider a Vulcanian-type scenario because i) field evidences suggest that the majority of VBPs associated with the Commenda unit are displaced, making any validation attempt impossible and ii) the caprock assumption used for the probabilistic sampling of eruption scenarios is valid only for Vulcanian eruptions.

We developed a Vulcanian-type scenario around the reference 1888–1890 eruption. ESPs were constrained based on data presented in Section 3.4 and the works of Bianchi (2007) and Tsunematsu (2012). Previous authors have estimated proportions of dense juvenile blocks, thin–rinded and thick–rinded breadcrust bombs to be respectively 70–90%, 5–15% and 10–20% of the total observerd VBPs. Since proportions of each VBP type obtained at the sampling site S2 (Fig. 1; Section 3.4) fall within these ranges (Mercalli and Silvestri, 1891; Bianchi, 2007; Di Traglia, 2011), we assume a proportion of 80% of lithic blocks, 14% of thin–rinded and 6% of thick–rinded breadcrust bombs.

Probabilistic hazard assessments rely on the simulation of a large number of event, stochastically varying ESPs in order to account for the variability of eruptive processes when predicting future eruptions. Table 3 summarizes the ESPs for the Vulcanian eruption scenario at La Fossa. Variable parameters include i) density ($kg \cdot m^{-3}$), ii) VBP diameter (ϕ), iii) ejection velocity ($m \cdot s^{-1}$) and iv) ejection angle (° from vertical). The number of observations being too limited to estimate complex probability distributions (e.g. based on Tsunematsu, 2012, $n = 12$ for density measurements and $n = 40$ for diameter measurements), we used Gaussian distributions centred on the mean value (μ) and expressing the uncertainty using the standard deviation (σ), which accounts for about 68.3% of the population.

Table 3
Eruption source parameters associated with a Vulcanian–type eruption scenario at La Fossa volcano based on the 1888–1890 eruption. Different Gaussian distributions of densities are identified for [a] lithic blocks, [b] thin-rinded and [c] thick-rinded breadrcrust bombs.

		Unit	Mean	σ
Source	Density	$kg\ m^{-3}$	2500	100[a]
			800	50[b]
			1600	200[c]
	Diameter	ϕ	−7.65	1.2
	Velocity	$m \cdot s^{-1}$	100	50
	Ejection angle	rad	0	π/12
	Number particles	–	10^6	–
Wind	Speed	$m \cdot s^{-1}$	0	–
	Direction	Degree	0	–
Drag	Time step	s	0.01	–
	Pressure	hPa	1.01325×10^5	–
	Temperature at sea level	°K	298	–
	Thermal lapse	$°C\ km^{-1}$	-6.5×10^{-3}	–
	Reduced drag radius	m	200	–

The density associated with various types of VBPs was discretized in three different ranges. Separate runs were performed for each VBP type by i) adjusting the density range and ii) scaling the number simulated particles to reproduce the proportions of each VBP type. The mean densities and associated standard deviations of blocks, thin-rinded and thick-rinded breadcrust bombs were set to 2300 ± 100, 800 ± 50 and 1600 ± 200 kg·m^{-3}, respectively. The diameter is expressed on a Gaussian distribution in ϕ units, which results in a log–normal distribution when converted to metres. The mean diameter considered is -7.65ϕ (i.e. 0.2 m) with a $\sigma_{Diam} = 1.2\phi$. In metres, the $\mu - \sigma$ and $\mu + \sigma$ are 0.09 and 0.46 m, respectively. The median ejection velocity was set to 100 m·s^{-1} with a $\sigma_{Vel} = 50$ m·s^{-1}, which scales with published values for Vulcanian eruptions (Druitt et al., 2002; Alatorre-Ibargüengoitia et al., 2006; Wright et al., 2007; Alatorre-Ibargüengoitia et al., 2012; Maeno et al., 2013). The ejection angle was defined as a mean value centred on the vertical with a standard deviation of $\frac{\pi}{12}$ rad, i.e. 15°.

A standard atmosphere, no wind and a radius of reduced drag of 200 m were used to calculate drag forces (Mastin, 2001). Alatorre-Ibargüengoitia et al. (2012) report heights of about 600 m at Popocatepetl volcano, which we chose to reduce since these explosions appear larger and characterized by higher ejection velocities and distances reached by VBPs. Additionally, as discussed in Section 3.4, the radius drag is of limited importance in such proximal distances to the vent (Fig. 2). It is however important to notice that in the case of La Fossa, an altitude of 200 m above the vent is higher than the surrounding crater rim.

4.2. Probabilistic hazard assessment

The destructiveness caused by VBPs is mostly due to the high kinetic energy at impact; the aim of this hazard assessment is thus to investigate the probability to exceed critical energy thresholds. Various thresholds, hereafter expressed as E_T (J), were identified as potential threats to the built environment (e.g. Pomonis et al., 1999; Spence et al., 2005; Jenkins et al., 2014) and will be discussed later. Since VBPs result in discontinuous punctual impacts, it is necessary to average the number of impacts on a representative area. We explore two different approaches to quantify the hazard related to VBPs impacts.

4.2.1. Pixel-based approach

First, we average the VBP impacts on an equally–spaced grid. The probability of occurrence of a VBP of a given energy threshold E_T in a pixel i,j of area A is quantified as:

$$P(A_{i,j}, E_T) = \frac{\sum VBP_{A_{i,j},E_T}}{n_{VBP}}, \quad (10)$$

where n_{VBP} is the total number of simulated VBPs.

Since this approach introduces a dependency to the pixel area, we assess the sensitivity of our post–processing method to i) the number of VBPs simulated and ii) the resolution of the grid used to compile probabilistic hazard assessments. The number of simulated VBPs was varied between 10^4 and 10^7 with increment of 10^1. Grid resolutions of 5, 10, 20, 50, 75, 100, 200, 300, 400, 500, 600, 700, 800, 900 and 1000 m were tested. 20 simulations were performed for each combination of number of particles/grid resolution. The probability to exceed an impact energy of 4000 J was computed for the top of the hiking path, the center of the Porto area and Porto di Ponente (green points 1, 2, and 3 on Fig. 1, located 400, 1300 and 1700 m from the vent, respectively). This threshold represents the minimum energy to penetrate weak RC slabs roofs (Spence et al., 2005).

Fig. 3 summarizes the sensitivity analysis. For a given combination of number of particles/grid resolution, we assess the sensitivity based on the mean probability $P(A_{i,j}, 4000\text{ J})$ (i.e. left y axis) and the associated standard deviation (right y axis) calculated over the 20 simulations. The x axis represents the resolution of the equally spaced grid, where the pixel area A is the square of the grid spacing. Each column of plots contains results for a different location, with distance from the vent increasing from left to right (Fig. 1). Rows from top to bottom represent an increase of the number of simulated particles. Results show that:

- For a given point, an increase of the number of simulated particles does not significantly affect the mean probability value but greatly reduces the associated standard deviation;
- For a given number of simulated particles, the probability decreases with distance from the vent but the standard deviation remains in the same order of magnitude;
- For the proximal point (i.e. Point 1 in Fig. 3), a change of order of magnitude of mean probabilities (i.e. 10^{-2}% to 10^{-1}%) occurs at a resolution of about 200 m.

Based on these observations, we simulate 10^6 particles averaged on a 100×100 m grid, which provides a compromise between computation time and accuracy of the output. In the absence of a plateau with stable probability values, we fix the resolution threshold in the zone of the lowest variability of mean probability values.

4.2.2. Zone-based approach

Second, we assess the probability of impact in a zone of interest Z. Here, such a zone is defined either as a distance from the vent (i.e. the probability of impact at a given distance interval from the vent) or as a radial sector (i.e. probability of impact at a given azimuth interval from the vent). Probabilities of a VBP exceeding an energy threshold E_T can then be normalized either on the total number of VBPs simulated or on the number of VBPs that fell in a given zone Z. In the first case, $P(Z, E_T)$ answers the question "what is the probability of a VBP to exceed a given energy threshold E_T in a zone Z?". In the second case, $P(E_T|Z)$ answers the question "knowing that a VBP impacts the zone Z, what is its probability to exceed an energy threshold E_T?".

Note that although the combination of both approaches might result in an overall picture of the VBP hazard around a given volcano, the comparison of the hazard with other volcanoes is difficult due to the nature of both the modelling and the post–processing methods. Additionally, each approach to the probabilistic quantification of the VBP hazard have different purposes. For instance, the zone–based approach is more suitable for hazard zoning purposes, whereas the pixel–based approach is more appropriate for impact assessment purposes. For this reason, this latter one will be discussed in more details in this paper, but the zone–based approach is thoroughly presented in the user–manual of the GBF model.

4.3. Vulnerability of the built environment

The high kinetic energy of VBPs can result in damages to the structures, roof perforation or collapse of the building (Blong, 1984; Pomonis et al., 1999; Spence et al., 2005; Jenkins et al., 2014). The likelihood of a building to suffer damages is typically expressed by vulnerability curves describing the relationship between the intensity of the hazard and the probability of damage. Such a relationship is commonly defined through a combination of i) post-event damage studies (e.g. Pomonis et al., 1999; Blong, 2003b; Wilson et al., 2011), ii) laboratory experiments and iii) theoretical studies on material strengths (e.g. Petrazzuoli and Zuccaro, 2004). Volcanic eruptions being multi–hazard systems, each hazard requires different vulnerability function. In the case of tephra fallout, such a function describes the relationship between tephra load and impact. For VBPs, the parameter of importance is the kinetic energy at the impact.

Here, we assess the vulnerability of buildings to roof perforation from VBP impacts. The starting point of this study is the vulnerability curves proposed by Spence et al. (2005) for the tephra hazard in Europe. Vulnerability curves take the shape of a cumulative density

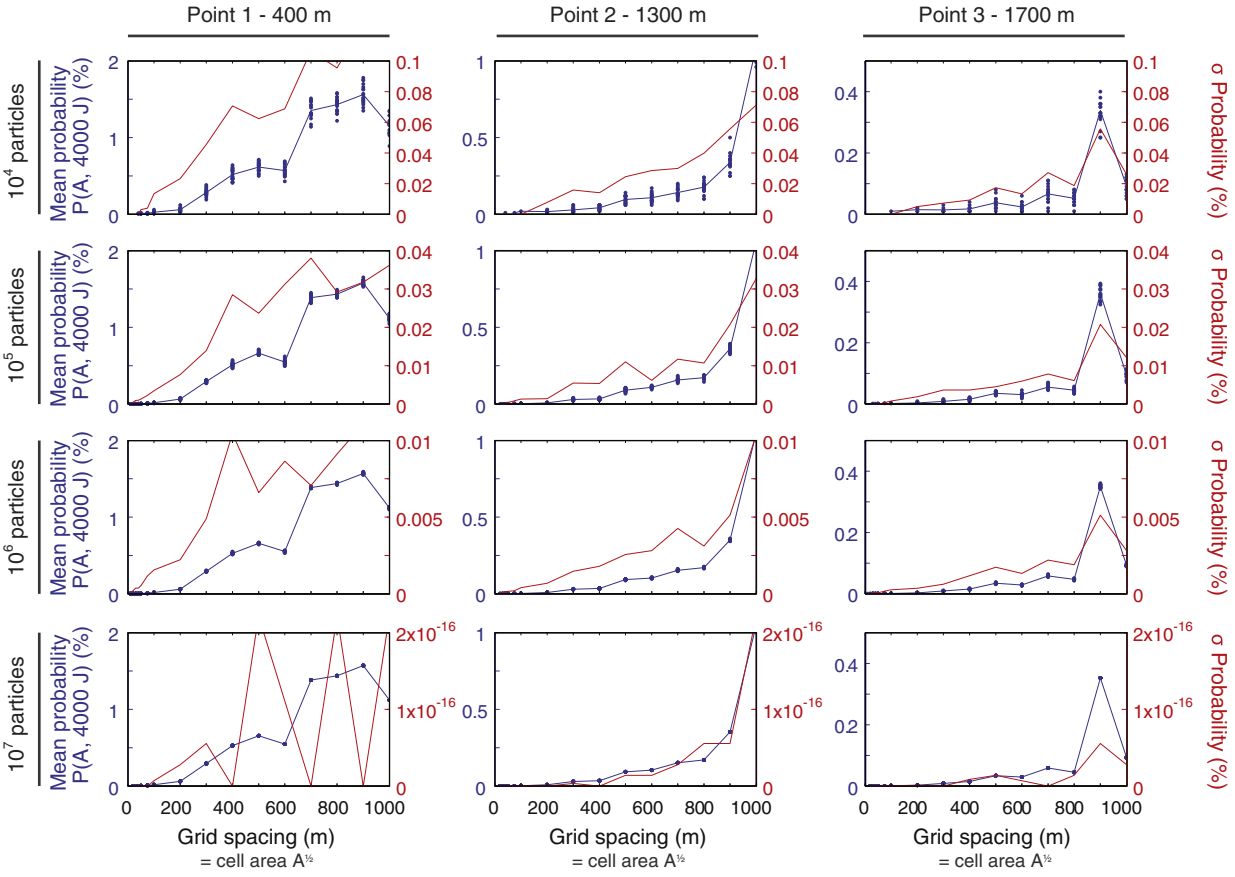

Fig. 3. Sensitivity of the probabilistic hazard assessment strategy to i) the number of simulated particles and ii) the resolution of the grid used to quantify the probability of VBPs exceeding a given energy threshold E_T of 4000 J. Across sub-plots, the rows represent variable number of simulated particles and the columns represent the different points on which probabilities were calculated (i.e. green points in Fig. 1) and include the top of the hiking path (Point 1; 400 m from the vent), the center of the Porto area (Point 2; 1300 m from the vent) and Porto di Ponente (Point 3; 1700 m from the vent). Each plot has two y-axes: the left one (blue) shows the mean probability calculated over the 20 simulations (blue dots) for each set of number of particles/grid resolution; the right one (red) shows the corresponding standard deviation.

function of a Normal distribution (ϕ) and are expressed as a function of the mean kinetic energy E_{mean} and σ. Following Spence et al. (2005) and Jenkins et al. (2014), the probability of perforation ($P_{perforation}$) is expressed as a function of the VBP energy I (J) with the following relationship:

$$P(Perforation|I) = \phi(ln(I), ln(E_{mean}), \sigma). \quad (11)$$

Two aspects require care when Eq. (11) is used. Firstly, although ϕ represents the standard form of a cumulative density function of a Normal distribution, both I and E_{mean} are expressed in natural logs, which results in a log-normal distribution (Spence et al., 2005). Secondly, although σ is often referred to as *standard deviation*, which suggests that it has the same unit as the mean, it is in fact a coefficient of variation expressed between 0 and 1. Therefore, when Spence et al. (2005) suggest that "σ is 20% of the mean", it implies the use of a coefficient of variation of 0.2.

Biass et al. (2016) provide a review of the built environment in Vulcano. The 2000 census of the Italian National Institute for Statistics (ISTAT, 2005) identifies 1093 buildings on the island, comprising 895 residential houses and 64 public and tourism facilities. According to this census, the main construction period spans from the 1970's to 1980's, but discussions with inhabitants and workers on the island suggest that most buildings were renovated over the years, making the true period of construction difficult to assess. Additionally, the field survey performed in the context of the EU-funded *ENSURE* project (Bonadonna et al., 2011) provides detailed descriptions of the most representative building in a 100×100 m pixel, revealing that building morphologies are homogeneously distributed over the settled areas and include 70% single–storey buildings, 73% with flat roofs and 54% with a regular morphology. Additionally, building's footprints were mapped from aerial images (Bonadonna et al., 2011).

Here, we adapted the method of Spence et al., 2005 for the specific case of Vulcano and for the VBP impact. Firstly, following Biass et al. (2016), we assume that buildings either have flat reinforced concrete roofs or tiled roofs over a timber structure in good or average conditions. These observations were compared with those of Spence et al. (2005) to define the roof classes in Table 4. Secondly, vulnerability curves of Spence et al. (2005) were adapted to express the probability of roof perforation as a function of the kinetic energy at impact. We estimated the mean energies E_{mean} of each roof class (Eq. (11)) based on published literature (e.g. Blong, 1984; Pomonis et al., 1999; Spence et al., 2005;

Table 4
Description of the typical roofing stocks of Spence et al. (2005) adapted to the built environment of Vulcano (adjusted from Biass et al., 2016). The vulnerability of each roof class is characterized by a mean kinetic energy E_{mean} and a standard deviation σ fixed to 0.2. The E_{mean} is identified based on existing literature. *RC* stands for reinforced concrete.

Roof class	Description	E_{mean} (J)
WE (weak)	Tiled roof, poor condition	60
MW (medium weak)	Tiled roof, average or good condition	100
MS (medium strong)	Flat RC roof, average condition	4000
ST (strong)	Flat RC roof, good condition	8000

Tsunematsu, 2012; Jenkins et al., 2014). Following the approach applied to tephra fallout, the standard deviation of the distribution (σ) was fixed to 0.2 (Spence et al., 2005; Jenkins et al., 2014). Fig. 4 illustrates the vulnerability curves for the roof classes defined in Table 4.

5. Results

For the scenario identified in Table 3, Fig. 5A shows the variation of the median VBP energy with distance from the vent, with the associated variability expressed as the 25th–75th percentiles and the 2nd–98th percentiles. Two main observations must be outlined from Fig. 5A. Firstly, the median energy increases with distance from the vent, which is a consequence of the caprock assumption used to model Vulcanian explosions (Self et al., 1979; Wilson, 1980; Fagents and Wilson, 1993). Such an assumption implies that once the coherent plug reaches its fragmentation level (here considered as the reduced drag radius in Table 3), all VBPs are released with the same ejection velocity, regardless of their masses. As a result, only large VBPs possess a sufficient kinetic energy to reach distances far away from the vent and are therefore associated with relative high impact energies. Secondly, curves in Fig. 5A follow a smooth trend up to a distance of ~3000 m (i.e. vertical dashed line in Fig. 5), after which they become chaotic. Projecting this distance on Fig. 5B suggests that only 10^3 particles are falling at distances larger than ~3000 m (i.e. 0.1% of the total number of simulated VBPs), which is too limited to obtain stable results. Probabilities calculated for distances from the vent larger than ~3000 m should thus be critically used.

5.1. Hazard assessment

We start by quantifying the probability of a VBP impact to exceed energy thresholds hazardous for roof perforation. Note that probabilities expressed here are based upon the conditional probability of occurrence of the associated eruption scenario. Following the pixel–based approach, Fig. 6A–B shows the geographical distribution of probabilities to exceed kinetic energies of 60 J (i.e. threshold for the perforation of tiled roofs in poor condition) and 8000 J (i.e. threshold for the perforation of reinforce concrete roofs in good condition). Impacts are averaged on a 100 × 100 m pixel and normalized over the total number of simulated VBPs. Following the zone–based approach, we estimate probabilities of impact at a given distance from the vent (Fig. 7A–B) or at a given radial sector around the vent (Fig. 7C–D). Probabilities are expressed either as normalized over the total number of simulated VBPs (i.e. $P(Z,E_T)$; Fig. 7A,C) or as normalized over the number of VBPs that impacted the considered zone (i.e. $P(E_T|Z)$; Fig. 7B,D). Finally, hazard curves were compiled (Fig. 8), which show the probability of exceeding any impact energy for the settled areas of Porto, Il Piano, Lentia and Vulcanello (white squares in Fig. 1 and Fig. 6), located respectively 1.3, 2.4, 1.8 and 2.6 km away from the vent.

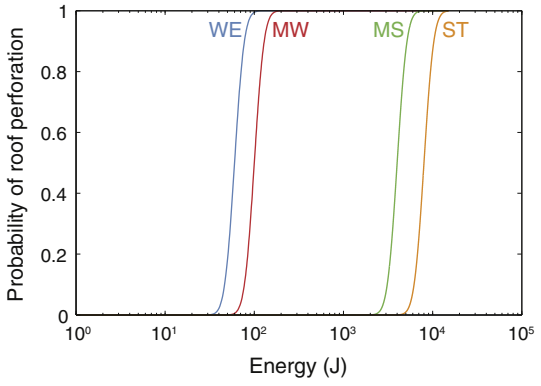

Fig. 4. Vulnerability curves for the roof types *WE*, *MW*, *MS* and *ST* of Spence et al. (2005) as defined in Table 4.

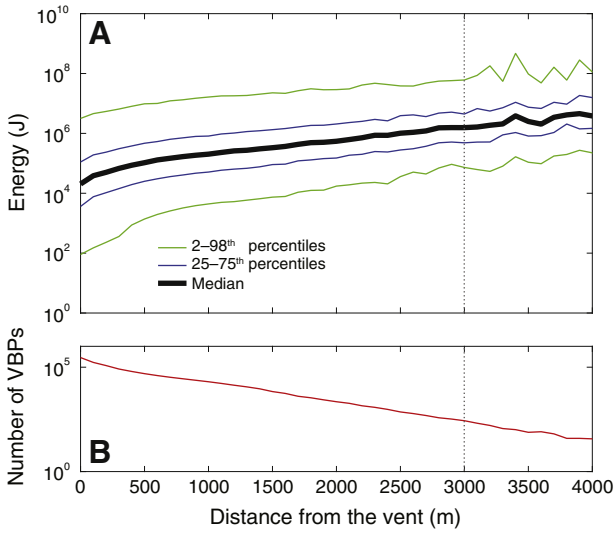

Fig. 5. A: Median energy with distance from the vent. The uncertainty is expressed by the 25th–75th and the 2nd–98th percentiles. The vertical dashed line indicates the distance (i.e. ~3000 m) at which the number of particles is too limited to produce stable results. B: Number of particles with distance from the vent, suggesting that only ~10^3 VBPs fall beyond a distance of ~3000 m.

Fig. 6A–B suggest little difference in the final probability values for the energy thresholds considered for the built environment on Vulcano. This observation is confirmed by Fig. 8, which shows almost constant probability values up to critical energy thresholds of 10^4 J for Porto and Lentia and 10^5 J for Vulcanello and Piano. As a result, probabilities presented throughout this section are equal for all energy thresholds relevant for the built environment of Vulcano. Porto (1.3 km N of the vent) and Lentia (1.8 km NW of the vent; Fig. 1) are the most exposed settlements with probabilities of ~10^{-2}% and ~5×10^{-3}%, respectively. The settlements of Il Piano and Vulcanello, located at respectively 2.4 km SW and 2.6 km N of the vent (Fig. 1) result in probabilities of 7×10^{-4}% and 4×10^{-4}%.

Using the zone–based approach to assess the probability of impact at a given distance from the vent (Fig. 7A–B), the choice of the type of probability (i.e. $P(Z,E_T)$ vs $P(E_T|Z)$) greatly influences the meaning of the probabilistic hazard assessment. When normalized over the total number of simulated VBPs, Fig. 7A shows greater probabilities of being impacted by a VPB with a kinetic energy of 4000 J in proximal area, where a probability of ≥10% exists up to a distance of 1 km away from the vent. In contrast, Fig. 7B shows that should a VBP impact a given distance interval, there is a larger probability that it will exceed a kinetic energy of 4000 J at larger distances from the vent. As a result, there is a ~100% probability that a VBP will exceed 4000 J from a distance of 1 km from the vent. When a similar approach is applied on zones of interest defined as radial sectors around the vent, Fig. 7C shows slightly higher probabilities of the NNW sector to be impacted by VBPs ($P(Z,E_T)$ of 5–15%), which corresponds to the lowest part of the crater rim. Fig. 7D shows that should a VBP impact any radial sector, there is a ≥90% probability that it will exceed an energy of 4000 J.

Probabilistic energy maps (Fig. 6C–D) quantify the energy occurring at a given probability threshold. At each pixel, the 10th, 25th, 50th, 75th and 90th percentiles were calculated over the energy of all VBPs that fell in a given 100 × 100 m area. Since the *n*th percentile returns the lowest *n*% of the population, there is a 100 − *n*% probability that the energy will exceed the energy given by the *n*th percentile. As an illustration, the 10th percentile of a given pixel shows the energy occurring with a 90% probability within this given pixel. Note that this energy is based upon the conditional probability that a VBP impact is occurring inside this pixel, and does not consider the probability of the pixel to be impacted. Fig. 6C–D illustrate the geographical distributions of energies

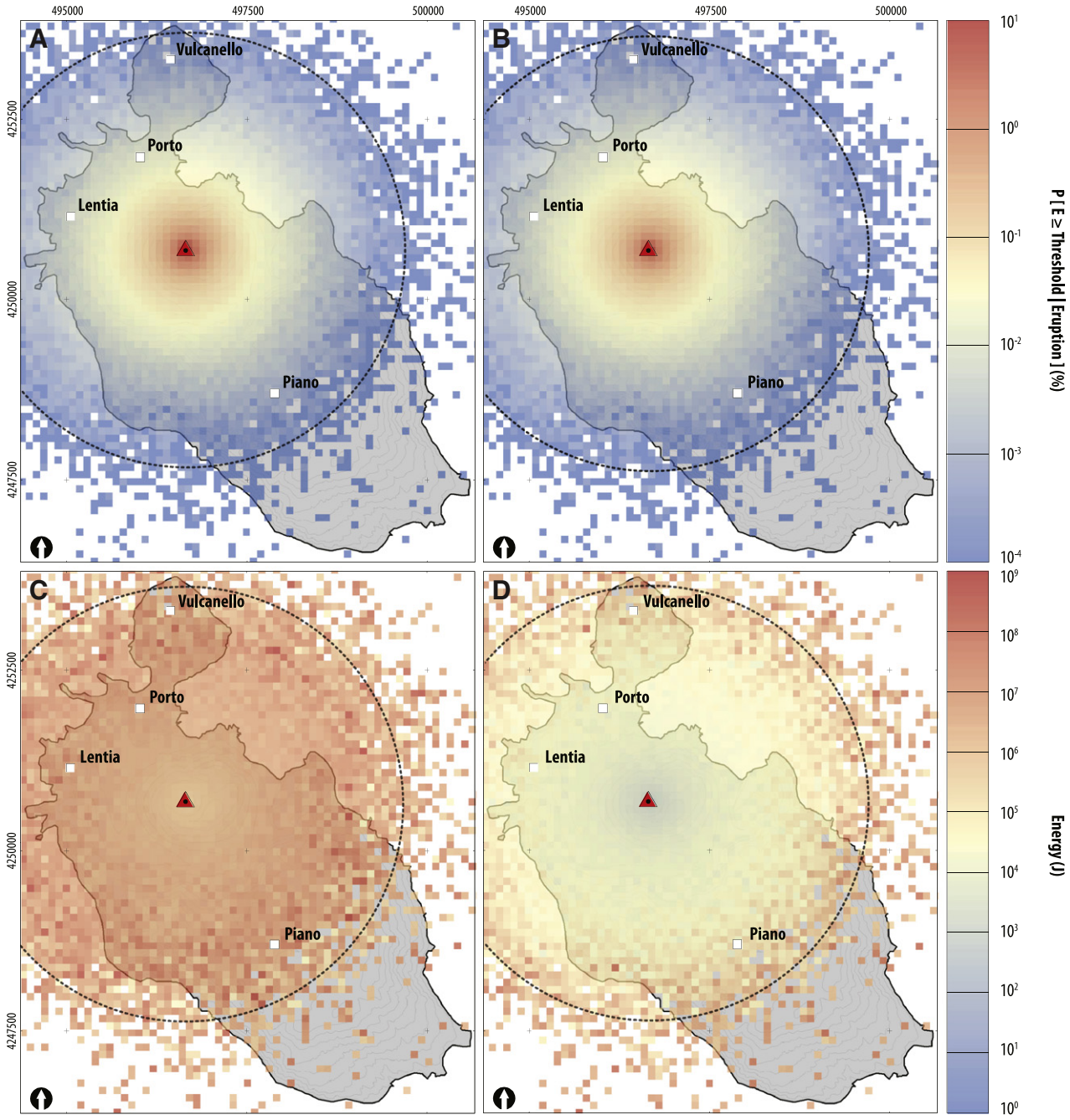

Fig. 6. A–B: Probability maps (%) of VBPs exceeding energies of (A) 60 J and (B) 8000 J. C–D: Energy maps for probabilities of occurrence within a given pixel of (C) 10% and (D) 90%. The main towns are shown as white squares. The black dashed line contours a distance of 3000 m around the vent, considered as the distance beyond which not enough particles are observed to provide stable results (Fig. 5). Probabilities are conditional to the occurrence of the eruption scenario.

for probabilities of occurrence of 10% and 90%, which result in typical kinetic energies of 10^6–10^7 and 10^4–10^5 J over Porto, respectively.

5.2. Pre-event impact assessment

The impact was assessed by combining the vulnerability analysis (Table 4 and Fig. 4) with the probabilistic energy maps (Fig. 6C–D). For each building, the energy occurring in the containing pixel is retrieved and used in Eq. (11) to calculate the probability of roof perforation. Two observations can be made here. Firstly, Fig. 7A–B suggests similar probabilities to exceed VBP impacts of 60 J or 8000 J. This observation is supported by Fig. 8, that reveals identical probabilities of occurrence of impacts $<\sim 3\times10^3$ J for the localities of Lentia and Porto and $<\sim 10^5$ J for the Vulcanello and Piano. Secondly, Fig. 7C–D indicates that energies of $\sim 10^4$ J have a ≥90% probability of occurrence over the main localities. These joint observations suggest that for the case of Vulcano, the proximity to the active vent makes any VBP impact potentially critical for the built environment, reducing the need to consider various roof typologies or probabilities of occurrence.

Fig. 9 and Table 5 summarize the impact of VBPs on the built environment. Fig. 9 can be read as a box and whisker plot, in which black dots indicate raw composite probabilities of perforation of individual buildings ($n = 1093$) calculated assuming typical roof typologies of Spence et al. (2005) (x axis). The resulting distributions are displayed as the median (red line), the 25^{th}–75^{th} percentiles range (blue area) and the 10^{th}–90^{th} percentiles range (orange area). Fig. 9 shows how 90% of

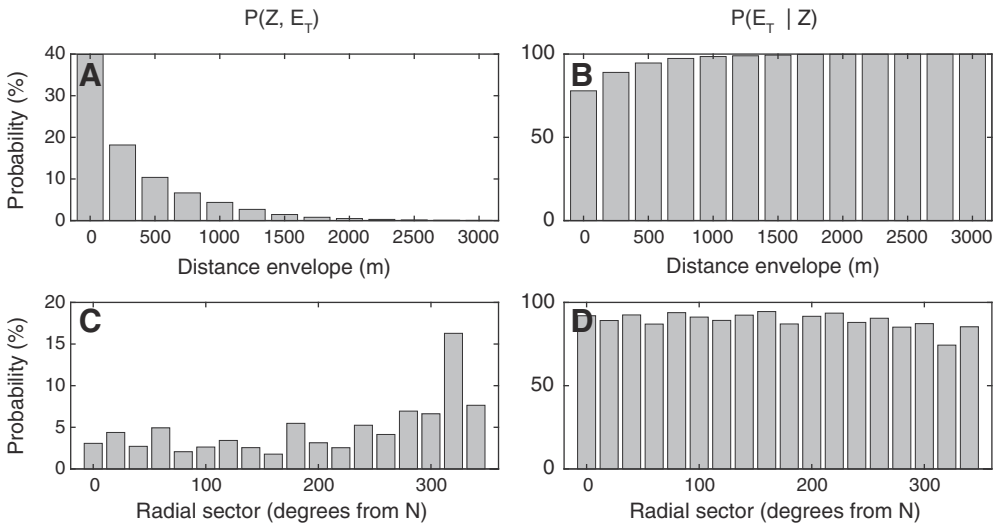

Fig. 7. Probabilities of VBPs to exceed a kinetic energy of 4000 J at a given distance from the vent (A–B) and a given radial sector around the vent (C–D). The left column expresses the probability normalized over the total number of simulated VBPs (i.e. $P(Z,E_T)$) whereas the right column is averaged over the number of VBPs that impacted the considered zone (i.e. $P(E_T|Z)$). Bin sizes are 250 m for the distance and 20 ° for the radial sectors.

the building stock of Vulcano (i.e. 90th percentile) has a probability of $\leq 4\times10^{-2}$% of roof perforation by VBP impact, regardless of the building type. Table 5 reports the same information.

6. Discussion

We introduce a new model called *Great Balls of Fire* designed for the probabilistic analysis of VBP impacts. The model relies on the identification of probabilistic eruption scenarios described by distributions of selected input parameters, namely i) initial ejection velocities and ii) size distribution and iii) densities of VBPs. Sets of post–processing functions are also provided to compile probabilities of VBP impacts exceeding hazardous thresholds of kinetic energies. Probabilities can be expressed on a pixel-based approach, suitable for hazard and pre–event impact assessments, or on zones of interests (either concentric circles around or radial sector around the vent), suitable for hazard zoning purposes.

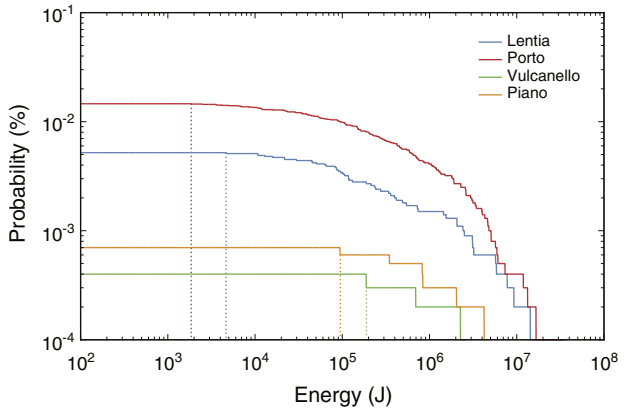

Fig. 8. Hazard curves for the urban settlements areas of Porto, Il Piano, Lentia and Vulcanello located 1.3, 2.4, 1.8 and 2.6 km away from the vent, respectively (white squares in Fig. 1 and Fig. 6). Vertical dashed lines show, for each location, the energy threshold below which impacts of any energy have equal probabilities of occurrence.

6.1. Probabilistic hazard assessment for VBPs

Hazard assessments for VBPs published in the literature follow two main approaches. Some authors used the *Eject*! model to estimate probability density functions of impact distances based on ESPs inferred from observed VBPs (e.g. Sandri et al., 2014). In contrast, other authors associate hazard zones based on deterministic eruption scenarios with their respective probabilities of occurrence (e.g. Alatorre-Ibargüengoitia et al., 2006; Alatorre-Ibargüengoitia et al., 2012). Here, we aim at providing a fully probabilistic assessment for VBP impacts that can be incorporated in Bayesian frameworks to produce long term multi–hazard assessments (e.g. Marzocchi et al., 2008; Selva et al., 2010; Sandri et al., 2014; Sheldrake, 2014; Thompson et al., 2015). The probabilistic approach adopted here is associated with a dependency on both the number of simulated VBPs and on the size of the zones of interest defined to average VBP impacts. This aspect should be investigated on a case-per-case basis, with the aim of finding the best compromise between computation time and output accuracy. For the example of La Fossa, Fig. 3 shows minimum discrepancies of mean and standard deviation values of probabilities from 10^6 simulated particles, which generates valid results up to a distance 3000 m away from the vent, shown as the dashed circle on Fig. 6. In contrast, 10^7 particles increase the confidence radius to about 3500 m, but results in both calculation and post-processing times multiplied by a factor 10.

6.2. Probabilistic eruption scenarios for VBPs

In probabilistic hazard assessments, eruption scenarios are typically expressed as distributions of the most critical ESPs for the modeled phenomenon (e.g. earthquake source parameters for seismic and tsunami hazard assessments, Geist and Parsons, 2006; volume for landslide hazard assessments, Guzzetti et al., 2005; thickness and volumes for lava flows, Connor et al., 2012). Alatorre-Ibargüengoitia et al. (2006) identified the total kinetic energy of Vulcanian explosions as the relevant ESP for defining eruption scenarios for VBPs, which can practically only be relevant when i) the ballistic model is coupled with a conduit model (e.g. Alatorre-Ibargüengoitia et al., 2012) and ii) when deterministic eruption scenarios are used.

Eruption scenarios as defined with our method differ from those presented by Alatorre-Ibargüengoitia et al. (2012) for Popocatepetl on two main aspects. Firstly, in our method, ESPs are those identified by

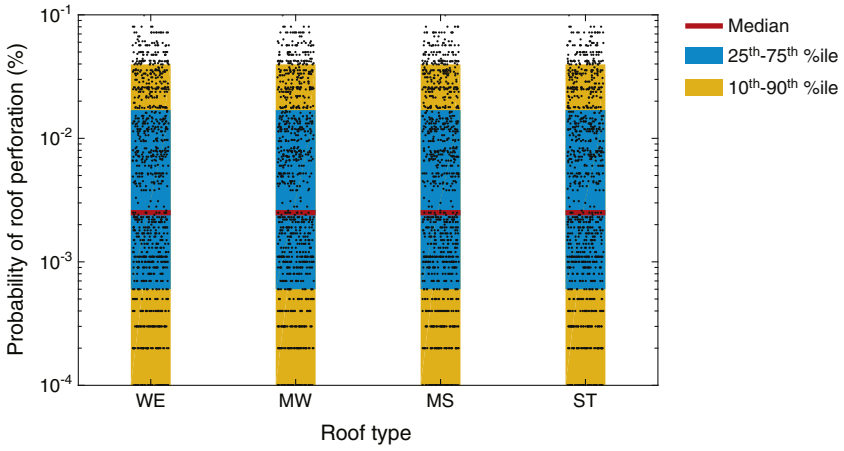

Fig. 9. Impact on the built environment expressed as a probability of roof perforation (y axis) for the various roof types of Spence et al. (2005). Black dots show the probability of roof collapse of each building assuming a given roof typology of Spence et al. (2005) (x axis). Distributions of probabilities over all buildings are summarized as the median (red line), the 25th–75th interval (blue box) and the 10th–90th interval (orange box). For visibility, the lower y axis was manually set to 10^{-4}%.

Mastin (2001), stochastically sampled on either Gaussian or uniform distributions (Table 3). Secondly, the hazard zones resulting from the hazard assessment of Alatorre-Ibargüengoitia et al. (2012) for Popocatepetl are a direct consequence of the eruption scenarios, and, for instance, the high-hazard zone is defined as the typical range reached by VBPs resulting from the most likely and least intense type of activity. This deterministic approach, although complementary to the probabilistic approach when the probability of a future eruption tends to 1 (Marzocchi et al., 2008), is of limited information for long-term planning and risk reduction strategies. As an example, the cone of Popocatepetl is mostly deserted within a radius of a few kilometres around the vent, and the purpose of a risk assessment for VBPs is mainly the delimitation of exclusion zones. In contrast, urban areas are found within a radius of 1 km around La Fossa and probabilistic approaches become a necessity to estimate the likelihood of occurrence of VBPs impacts as a first step towards the development and implementation of pro–active risk mitigation strategies.

6.3. Eruptive scenarios at La Fossa

We developed a scenario for typical long-lasting Vulcanian eruptions at La Fossa based on the inversion of field observations (Fig. 2) and the comparison with published literature (e.g. Alatorre-Ibargüengoitia et al., 2012; Fitzgerald et al., 2014; Tsunematsu et al., 2014). Using the caprock assumption, VBPs of different sizes have equal probabilities to be launched in the velocity range expressed in Table 3. Ejection velocities reported in the literature range from 30 to 400 $m \cdot s^{-1}$ (Fagents and Wilson, 1993; Mastin, 1995; Wright et al., 2007; Feeley and Winer, 2009; Alatorre-Ibargüengoitia et al., 2012; Fitzgerald et al., 2014). In the case of La Fossa, the distribution was assumed Gaussian with values of mean and standard deviations of 100 and 50 $m \cdot s^{-1}$, respectively, which implies that 95% of the VBP's will result in ejection velocities comprised between >0 and 200 $m \cdot s^{-1}$, respectively. We argue that this range is justifiable because i) it covers the majority of ejection velocities identified for other volcanoes while discarding sub- or supersonic velocities that are unlikely at La Fossa and ii) agrees with ranges obtained through inversion of field data (Fig. 2). The size distribution of VBPs is described here by a Gaussian distribution in ϕ units (i.e. a log-normal distribution is metres).

At La Fossa, the 1888–1890 eruption was characterized by at least three populations of VBPs associated with different densities (Table 2). Our approach accounts for three different populations of densities, weighing the number of simulated VBP according to proportions of occurrence of each VBP type observed in the field. However, observations of Mercalli and Silvestri (1891) suggest that each VBP type was produced at different stages of the two-year-long Vulcanian cycle. Outcomes of our probabilistic hazard assessment do not capture the evolution of VBP type through time and should be viewed as a time-integrated hazard over the duration of a Vulcanian cycle.

Table 5
Final pre-event impact assessment showing the probability of roof perforation calculated at given percentiles on the distributions shown in Fig. 9. For instance, the 10th percentile shows that 10% of the building stock has a $\leq 1.0\times10^{-4}$% probability of roof perforation.

Percentile	Probability (%)
10th	1.0×10^{-4}
25th	6.0×10^{-4}
50th	2.5×10^{-3}
75th	1.7×10^{-2}
90th	4.0×10^{-2}

6.4. VBP hazard for Vulcano

At La Fossa, Fig. 6A–B suggest that all VBPs are likely to exceed energies critical for the strongest building typology. Energies of 60 J and 8000 J have maximum probabilities of occurrence of 17% and 11%, respectively, and a minimum probability of 10^{-4}% (Fig. 6) is constrained by the number of simulated particles and occurs when a given pixel is impacted by one single VBP. Such low probabilities are a consequence of the VBP hazard occurring on discrete points, which contrasts with the continuous blanketing caused by tephra fallouts. For tephra fallout, a probability of 100% occurs in a given pixel when all simulated eruptions result in deposits exceeding a critical threshold of tephra accumulation. In contrast, when considering VBPs, an hypothetical probability of 100% would imply that all simulated particles fell into a single pixel with energies exceeding a critical energy threshold. As a result, although Biass et al. (2016) show an average probability 15–30% to exceed critical accumulations of tephra for collapse of the weakest roofs in the Porto area, probabilities of occurrences of VBPs with critical energies for the built environment are of about 10^{-2}%. When probability maps are converted to energy maps (Fig. 6), our results show a probability of occurrence of high energies increasing with distance from the vent. For the case of a steam–blast eruption, Dellino et al. (2011) suggest a zone of maximum energy of 10^6 J extending 200 m from the vent. Our probabilistic approach suggests that in the

case of a Vulcanian eruption, such an energy has a 90% probability to be exceeded within a radius of 3000 m around the vent.

The southern flank of the 391 m-high cone of La Fossa is surrounded by a caldera rim rising from 250 to 400 m a.s.l. From the DEM, the height of the actual crater was estimated at ~220 m, and GBF simulations were performed with a 200 m-high region of reduced drag (Table 3). As a result, although Fig. 7 reveals a slight increase of probabilities towards NNE, our hazard assessment shows that the island does not host significant topographic barriers to shelter from VBPs, leaving only the southernmost part of the island with a virtually null probability of impact. On the other hand, the close proximity of the studied area to the source vent greatly reduces the influence of the radius of reduced drag on the final probabilities.

Biass et al. (2016) presents a study of wind patterns for the period 1980–2010 inferred from the ECMWF ERA- Interim database (Dee et al., 2011), which reveals a ~70% probability of wind directed towards SE at sea level, with associated velocities rarely higher than 20 m s^{-1}. To test the influence of wind on the final probabilistic hazard assessment, simulations were run with a mean wind with a constant velocity of 20 $m \cdot s^{-1}$ and a constant wind direction (i.e. provenance + 180 °) of 135 °. Results show that the final probabilities are not significantly affected by wind conditions. This is due on one side to the fact that smaller particles will be more influenced by wind forces, which will necessarily fall relatively close to the vent due to the caprock assumption. In this case the large number of particles falling in proximal area is the dominant influence on the final probability values. On the other side, only a limited number of large particles will impact more distal areas, but since wind has little effect on them, their additional displacement is not sufficient to affect the final probability values.

6.5. Pre-event impact assessment

In our impact assessment, the physical vulnerability only describes the likelihood of roof perforation resulting from a dynamic impact. This implies that the risk considered here regards a potential loss of life (e.g. Spence et al., 2005; Jenkins et al., 2014) rather than expressing the loss of economical value (e.g. Blong, 2003a). A comprehensive impact assessment on the built environment should include not only roof perforation but also aspects such as structure collapse and impacts on walls. Additionally, our analysis does not consider the physical impact on lifelines, nor attempts to quantify the systemic repercussions of the physical impact on critical infrastructures identified in Fig. 1. Nevertheless, this work is a first steps towards a holistic risk assessment that systematically includes a component of impact within probabilistic studies of the volcanic hazards.

Following Biass et al. (2016), the vulnerability of the built environment was based on the typical building types of Spence et al. (2005), extrapolated to dynamic impacts following two main assumptions. Firstly, the limited observations of damages related to VBPs impacts does not allow to develop robust vulnerability curves. In natural hazards, the closest analogous phenomena associated with impacts at high kinetic energies include hail storms and rockfalls (e.g. Andrews and Blong, 1997; Hohl et al., 2002; Agliardi et al., 2009; Mavrouli and Corominas, 2010b; Mavrouli and Corominas, 2010a). Resulting vulnerability curves can take various shapes such as sigmoid (e.g. Agliardi et al., 2009) and logistic (e.g. Hohl et al., 2002) shapes. Here, in the absence of more detailed information, we follow the approach undertaken for tephra fallout (e.g. Pomonis et al., 1999; Spence et al., 2005; Jenkins et al., 2014) using a lognormal distribution and a fixed coefficient of variation of 0.2. Secondly, published post–event impact assessments report VBP impacts associated with variable energy thresholds (e.g. Blong, 1984; Pomonis et al., 1999; Blong, 2003b). Here, we estimated mean energy thresholds for the built environment on Vulcano by comparing observed impacts with typology of buildings resulting from our field survey (Biass et al., 2016). As a result, two end-members of vulnerability to VBPs were identified comprising tile roofs on the weakest spectrum and reinforced concrete roofs on the strongest. Fig. 4 reflects this bipolarity due to critical energy thresholds varying by orders of magnitude between the two families of roofs identified in Vulcano (i.e. tiles and reinforced concrete; Table 4). However, due to the proximity of the built environment to the eruptive vent, there is an equally high probability of impact at Vulcano regardless of the roof type.

In terms of cascading effects between volcanic hazards, the relationship between VBPs and tephra is ambiguous. On one hand, tephra can act as a blanket absorbing energy from a VBP and thus reduce it propensity to perforation from a dynamic impact. On another hand, VBPs can increase the static load already caused by tephra layers and contribute to roof collapse. These complex vulnerability patterns occurring in the context of multi–hazards risk assessments were already discussed by Zuccaro et al. (2008) and underline the complex task of combining vulnerability curves for different natures of hazards (i.e. static load vs. dynamic impact) potentially simultaneously affecting exposed elements.

7. Conclusion

A new approach for the hazard assessment related to the ejection of VBPs is introduced, which quantifies the probabilities of occurrence of VBP impacts exceeding hazardous thresholds of kinetic energy. This approach, in line with recent efforts to quantify volcanic hazards in terms of probabilities, relies on a new ballistic model called *Great Balls of Fire*, with the main features being:

- The definition of ESPs in terms of probability distributions;
- A variable drag coefficient;
- A fast computation time;
- The possibility to work on single CPUs or clusters of computers;
- Platform independent.

The model is distributed under a GPL3 licence and is available on *GitHub* (https://github.com/unigeSPC/gbf) along with post–processing functions and the user manual. It was validated using field observations of VBPs associated with the 1888–1890 eruption of La Fossa volcano. Additionally, sets of *Matlab* functions are provided to post process the model output into probabilistic hazard assessments for VBPs, resulting in a format useful for the integration in various GIS environments.

A generic Vulcanian eruption scenario was identified for La Fossa based on the stratigraphy of the last 1000 years. Results show that the settlements of Lentia and Porto are the most likely to be impacted by VBP, whereas Vulcanello and Piano are relatively safer (Fig. 4). In addition, the vulnerability of the built environment was assessed by extrapolating the generic tephra fallout vulnerability curves for European roofs of Spence et al. (2005) to the impact of VBPs based on a review of critical energy thresholds found in the literature along with a field survey of the built environment on Vulcano. Both hazard and vulnerability aspects were then combined to produce a first-order pre-event impact assessment in terms of potential number of affected buildings. Results show a high vulnerability of the built environment to the VBP hazard, and half of the building stock has a $\geq 2.5 \times 10^{-3}$% probability of roof perforation.

Acknowledgements

We are grateful to C. Frischknecht, H. Monnard, A. Cuomo and I. Manzella for providing the results of the building survey, to A. Galderisi for the building shapefiles, to L. Chevalley et C. Haenggeli for their help in the characterization of the built environment, to G. Bagheri, S. Jenkins and L. Pioli for the insightful comments and to J.L. Lewis for a great name. Computations were performed at University of Geneva on the Baobab cluster. S. Biass was supported by a SNF grant (200021-129997).

References

Agliardi, F., Crosta, G.B., Frattini, P., 2009. Integrating rockfall risk assessment and countermeasure design by 3D modelling techniques. Nat. Hazards Earth Syst. Sci. 9, 1059–1073.

Alatorre-Ibargüengoitia, M.A., Delgado-Granados, H., 2006. Experimental determination of drag coefficient for volcanic materials: calibration and application of a model to Popocatépetl volcano (Mexico) ballistic projectiles. Geophys. Res. Lett. 33, L11302.

Alatorre-Ibargüengoitia, M.A., Delgado-Granados, H., Farraz-Montes, I.A., 2006. Hazard zoning for ballistic impact during volcanic explosions at Volcán de Fuego de Colima (México). Geol. Soc. Am. Spec. Pap. 402, 209–216.

Alatorre-Ibargüengoitia, M., Scheu, B., Dingwell, D., Delgado-Granados, H., Taddeucci, J., 2010. Energy consumption by magmatic fragmentation and pyroclast ejection during Vulcanian eruptions. Earth Planet. Sci. Lett. 291, 60–69.

Alatorre-Ibargüengoitia, M., Delgado-Granados, H., Dingwell, D., 2012. Hazard map for volcanic ballistic impacts at Popocatépetl volcano (Mexico). Bull. Volcanol. 74, 2155–2169.

Andrews, K., Blong, R., 1997. March 1990 hailstorm damage in Sydney, Australia. Nat. Hazards 16, 113–125.

Arrighi, S., Tanguy, J.C., Rosi, M., 2006. Eruptions of the last 2200 years at Vulcano and Vulcanello (Aeolian Islands, Italy) dated by high-accuracy archeomagnetism. Phys. Earth Planet. Inter. 159, 225–233.

Bianchi, L., 2007. L'eruzione 1888–1890 di Vulcano (Isole Eolie):Analisi stratigrafica, fisica e composizionale dei prodotti. Unpublished msc thesis. Università di Pisa.

Biass, S., Scaini, C., Bonadonna, C., Folch, A., Smith, K., Höskuldsson, A., 2014. A multi-scale risk assessment for tephra fallout and airborne concentration from multiple Icelandic volcanoes — part 1: hazard assessment. Nat. Hazards Earth Syst. Sci. 14, 2265–2287.

Biass, S., Bonadonna, C., Traglia, F., Pistolesi, M., Rosi, M., Lestuzzi, P., 2016. Probabilistic evaluation of the physical impact of future tephra fallout events for the Island of Vulcano, Italy. Bull. Volcanol. 78, 1–22.

Blong, R.J., 1984. Volcanic hazards. A Sourcebook on the Effects of Eruptions. Academic Press, Orlando.

Blong, R., 2003a. A new damage index. Nat. Hazards 30, 1–23.

Blong, R., 2003b. Building damage in Rabaul, Papua New Guinea, 1994. Bull. Volcanol. 65, 43–54.

Bonadonna, C., 2006. Probabilistic modelling of tephra dispersion. Stat. Volcanol. 243–259.

Bonadonna, C., Biass, S., Manzella, I., Galderisi, A., Ceudech, A., Ferrara, F., Delmonaco, G., Menoni, S., Minucci, G., Belvaux, M., Manceau, J., Montfort-Climent, D., Sabourault, P., Foerster, E., 2011. Application of an integrated vulnerability conceptual approach Del. 5.3.3: Development of the Integrated Approach on the Vulcano case study. Tech. Rep. 212045, Ensure ProjectTechnical Report. ENSURE Project.

Cioni, R., Longo, A., Macedonio, G., Santacroce, R., Sbrana, A., Sulpizio, R., Andronico, D., 2003. Assessing pyroclastic fall hazard through field data and numerical simulations: example from Vesuvius. J. Geophys. Res. 108.

Connor, L., Connor, C., Meliksetian, K., Savov, I., 2012. Probabilistic approach to modeling lava flow inundation: a lava flow hazard assessment for a nuclear facility in Armenia. J. Appl. Volcanol. 1, 1–19.

De Astis, G., Volpe, L., Peccerillo, A., Civetta, L., 1997. Volcanological and petrological evolution of Vulcano island (Aeolian Arc, southern Tyrrhenian Sea). J. Geophys. Res. Solid Earth 102, 8021–8050.

De Astis, G., Lucchi, F., Dellino, P., La Volpe, L., Tranne, C.A., Frezzotti, M.L., Peccerillo, A., 2013. Geology, volcanic history and petrology of Vulcano (central Aeolian archipelago). Geol. Soc. Lond. Mem. 37, 281–349.

De Fiore, O., 1922. Vulcano (Isole Eolie). In: Friedlaender, I. (Ed.), Revisita Vulcanologica, pp. 1–393 (Suppl. 3).

De' Michieli Vitturi, M., Neri, A., Esposti Ongaro, T., Lo Savio, S., Boschi, E., 2010. Lagrangian modeling of large volcanic particles: application to Vulcanian explosions. J. Geophys. Res. Solid Earth 115, B08206.

Dee, D.P., Uppala, S.M., Simmons, A.J., Berrisford, P., Poli, P., Kobayashi, S., Andrae, U., Balmaseda, M.A., Balsamo, G., Bauer, P., Bechtold, P., Beljaars, A.C.M., van de Berg, L., Bidlot, J., Bormann, N., Delsol, C., Dragani, R., Fuentes, M., Geer, A.J., Haimberger, L., Healy, S.B., Hersbach, H., Hólm, E.V., Isaksen, L., Kållberg, P., Köhler, M., Matricardi, M., McNally, A.P., Monge-Sanz, B.M., Morcrette, J.J., Park, B.K., Peubey, C., de Rosnay, P., Tavolato, C., Thépaut, J.N., Vitart, F., 2011. The ERA-interim reanalysis: configuration and performance of the data assimilation system. Q. J. R. Meteorol. Soc. 137, 553–597.

Dellino, P., La Volpe, L., 1997. Stratigrafia, Dinamiche Eruttive e Deposizionali, Scenario Eruttivo e Valutazioni di pericolosità a La Fossa di Vulcano. Technical Report. CNR-Gruppo Nazionale per La Vulcanologia, Volume Speciale Vulcano-Progetto Triennale, pp. 1993–1995.

Dellino, P., Astis, G., Volpe, L., Mele, D., Sulpizio, R., 2011. Quantitative hazard assessment of phreatomagmatic eruptions at Vulcano (Aeolian Islands, Southern Italy) as obtained by combining stratigraphy, event statistics and physical modelling. J. Volcanol. Geotherm. Res. 201, 364–384.

Di Traglia, F., 2011. The Last 1000 years of Eruptive Activity at the Fossa Cone (Island of Vulcano, Southern Italy) (Ph.D. thesis) Università di Pisa.

Di Traglia, F., Pistolesi, M., Rosi, M., Bonadonna, C., Fusillo, R., Roverato, M., 2013. Growth and erosion: the volcanic geology and morphological evolution of La Fossa (Island of Vulcano, Southern Italy) in the last 1000 years. Geomorphology 194, 94–107.

Druitt, T.H., Young, S.R., Baptie, B., Bonadonna, C., Calder, E.S., Clarke, A.B., Cole, P.D., Harford, C.L., Herd, R.A., Luckett, R., Ryan, G., Voight, B., 2002. episodes of cyclic vulcanian explosive activity with fountain collapse at Soufrière Hills Volcano, Montserrat. In: Druitt, T., Kokelaar, B. (Eds.), The Eruption of Soufrière Hills Volcano, Montserrat, from 1995 to 1999 vol. 21. Geological Society of London, London, pp. 281–306.

Fagents, S.A., Wilson, L., 1993. Explosive volcanic eruptions—VII. The ranges of pyroclasts ejected in transient volcanic explosions. Geophys. J. Int. 113, 359–370.

Feeley, T.C., Winer, G.S., 2009. Volcano hazards and potential risks on St. Paul Island, Pribilof Islands, Bering Sea, Alaska. J. Volcanol. Geotherm. Res. 182, 57–66.

Fitzgerald, R., Tsunematsu, K., Kennedy, B., Breard, E., Lube, G., Wilson, T., Jolly, A., Pawson, J., Rosenberg, M., Cronin, S., 2014. The application of a calibrated 3D ballistic trajectory model to ballistic hazard assessments at Upper Te Maari, Tongariro. J. Volcanol. Geotherm. Res. 286, 248–262.

Fournier d'Albe, E.M., 1979. Objectives of volcanic monitoring and prediction. J. Geol. Soc. Lond. 136, 321–326.

Frazzetta, G., La Volpe, L., Sheridan, M.F., 1983. Evolution of the Fossa Cone, Vulcano. J. Volcanol. Geotherm. Res. 17, 329–360.

Frazzetta, G., Gillot, P.Y., Volpe, L., Sheridan, M.F., 1984. Volcanic hazards at Fossa of Vulcano: data from the last 6,000 years. Bull. Volcanol. 47, 105–124.

Fudali, R.F., Melson, W.G., 1971. Ejecta velocities, magma chamber pressure and kinetic energy associated with the 1968 eruption of Arenal volcano. Bull. Volcanol. 35, 383–401.

Geist, E.L., Parsons, T., 2006. Probabilistic analysis of tsunami hazards. Nat. Hazards 37, 277–314.

Gioncada, A., Mazzuoli, R., Bisson, M., Pareschi, M., 2003. Petrology of volcanic products younger than 42 ka on the Lipari–Vulcano complex (Aeolian Islands, Italy): an example of volcanism controlled by tectonics. J. Volcanol. Geotherm. Res. 122, 191–220.

Gonzalez, F.I., Geist, E.L., Jaffe, B., Kanoglu, U., Mofjeld, H., Synolakis, C.E., Titov, V.V., Arcas, D., Bellomo, D., Carlton, D., Horning, T., Johnson, J., Newman, J., Parsons, T., Peters, R., Peterson, C., Priest, G., Venturato, A., Weber, J., Wong, F., Yalciner, A., 2009. Probabilistic tsunami hazard assessment at Seaside, Oregon, for near- and far-field seismic sources. J. Geophys. Res. Oceans 114.

Gurioli, L., Zanella, E., Gioncada, A., Sbrana, A., 2012. The historic magmatic-hydrothermal eruption of the Breccia di Commenda, Vulcano, Italy. Bull. Volcanol. 1–20.

Guzzetti, F., Reichenbach, P., Cardinali, M., Galli, M., Ardizzone, F., 2005. Probabilistic landslide hazard assessment at the basin scale. Geomorphology 72, 272–299.

Heneka, P., Hofherr, T., 2011. Probabilistic winter storm risk assessment for residential buildings in Germany. Nat. Hazards 56, 815–831.

Hohl, R., Schiesser, H.H., Aller, D., 2002. Hailfall: the relationship between radar-derived hail kinetic energy and hail damage to buildings. Atmos. Res. 63, 177–207.

ISTAT, 2005. Progetto Census 2000 - Aggiornamento delle basi territoriali, descrizione dei dati. Technical Report.

Jenkins, S., Magill, C., McAneney, J., Blong, R., 2012. Regional ash fall hazard I: a probabilistic assessment methodology. Bull. Volcanol. 1–14.

Jenkins, S., Spence, R., Fonseca, J., Solidum, R., Wilson, T., 2014. Volcanic risk assessment: quantifying physical vulnerability in the built environment. J. Volcanol. Geotherm. Res. 276, 105–120.

Kaneko, T., Maeno, F., Nakada, S., 2016. 2014 Mount Ontake eruption: characteristics of the phreatic eruption as inferred from aerial observations. Earth Planets Space 68, 1–11.

Keller, J., 1980. The island of Vulcano. Rend. Soc. Ital. Mineral. Petrol. 36, 369–414.

Lewis, J.L., 1957. Great Balls of Fire, By Blackwell, O. and Hammer, J. Great Balls of Fire, Memphis, Sun Studio.

Maeno, F., Nakada, S., Nagai, M., Kozono, T., 2013. Ballistic ejecta and eruption condition of the vulcanian explosion of Shinmoedake volcano, Kyushu, Japan on 1 February 2011. Earth Planets Space 65, 609–621.

Marzocchi, W., Sandri, L., Selva, J., 2008. BET_EF: a probabilistic tool for long- and short-term eruption forecasting. Bull. Volcanol. 70, 623–632.

Mastin, L.G., 1995. Thermodynamics of gas and steam-blast eruptions. Bull. Volcanol. 57, 85–98.

Mastin, L.G., 2001. A simple calculator of ballistic trajectories for blocks ejected during volcanic eruptions. Technical Report. U.S. Geological Survey Open-File Report, pp. 01–45.

Mavrouli, O., Corominas, J., 2010a. B. Vulnerability of simple reinforced concrete buildings to damage by rockfalls. Landslides 7, 169–180.

Mavrouli, O., Corominas, J., 2010b. Rockfall vulnerability assessment for reinforced concrete buildings. Nat. Hazards Earth Syst. Sci. 10, 2055–2066.

Mendoza-Rosas, A.T., De la Cruz-Reyna, S., 2008. A statistical method linking geological and historical eruption time series for volcanic hazard estimations: applications to active polygenetic volcanoes. J. Volcanol. Geotherm. Res. 176, 277–290.

Mercalli, G., Silvestri, O., 1891. *Le* eruzioni dell'Isola di Vulcano incominciate il 3 agosto 1888 e terminate il 22 marzo 1890, relazione scientifica. Ann. Ufficio Centrale Metereol. Geodin. Ital. 10, 1–213.

Minakami, T., 1942. On the distribution of volcanic ejecta. (Part 1) the distributions of volcanic bombs ejected by the recent explosion of Asama. Bull. Earthquake Res. Inst. 20.

Petrazzuoli, S., Zuccaro, G., 2004. Structural resistance of reinforced concrete buildings under pyroclastic flows: a study of the Vesuvian area. J. Volcanol. Geotherm. Res. 133, 353–367.

Pistolesi, M., Donne, D., Pioli, L., Rosi, M., Ripepe, M., 2011. The 15 March 2007 explosive crisis at Stromboli volcano, Italy: assessing physical parameters through a multidisciplinary approach. J. Geophys. Res. 116.

Pomonis, A., Spence, R., Baxter, P., 1999. Risk assessment of residential buildings for an eruption of Furnas volcano, Sao Miguel, the Azores. J. Volcanol. Geotherm. Res. 92, 107–131.

Rosi, M., Pistolesi, M., Bertagnini, A., Landi, P., Pompilio, M., Di Roberto, A., 2013. Stromboli volcano, Aeolian Islands (Italy): present eruptive activity and hazards. Geol. Soc. Lond. Mem. 37, 473–490.

Sandri, L., Thouret, J.C., Constantinescu, R., Biass, S., Tonini, R., 2014. Long-term multihazard assessment for El Misti volcano (Peru). Bull. Volcanol. 76, 1–26.

Self, S., Wilson, L., Nairn, I., 1979. Vulcanian eruption mechanisms. Nature 277, 440–443.

Selva, J., Costa, A., Marzocchi, W., Sandri, L., 2010. BET_VH: exploring the influence of natural uncertainties on long-term hazard from tephra fallout at Campi Flegrei (Italy). Bull. Volcanol. 72, 717–733.
Sheldrake, T., 2014. Long-term forecasting of eruption hazards: a hierarchical approach to merge analogous eruptive histories. J. Volcanol. Geotherm. Res. 286, 15–23.
Spence, R.J.S., Kelman, I., Baxter, P.J., Zuccaro, G., Petrazzuoli, S., 2005. Residential building and occupant vulnerability to tephra fall. Nat. Hazards Earth Syst. Sci. 5, 477–494.
Steinberg, G.S., Lorenz, V., 1983. External ballistic of volcanic explosions. Bull. Volcanol. 46, 333–348.
Thompson, M., Lindsay, J., Sandri, L., Biass, S., Bonadonna, C., Jolly, G., Marzocchi, W., 2015. Exploring the influence of vent location and eruption style on tephra fall hazard from the Okataina Volcanic Centre, New Zealand. Bull. Volcanol. 77, 1–23.
Tsunematsu, K., 2012. New Numerical Solutions for the Description of Volcanic Particle Dispersal (Ph.D. thesis) University of Geneva.
Tsunematsu, K., Chopard, B., Falcone, J.L., Bonadonna, C., 2014. A numerical model of ballistic transport with collisions in a volcanic setting. Comput. Geosci. 63, 62–69.
Vanderkluysen, L., Harris, A., Kelfoun, K., Bonadonna, C., Ripepe, M., 2012. Bombs behaving badly: unexpected trajectories and cooling of volcanic projectiles. Bull. Volcanol. 74, 1849–1858.
Wilson, L., 1972. Explosive volcanic eruptions—II the atmospheric trajectories of pyroclasts. Geophys. J. Int. 30, 381–392.
Wilson, L., 1980. Relationships between pressure, volatile content and ejecta velocity in three types of volcanic explosion. J. Volcanol. Geotherm. Res. 8, 297–313.
Wilson, T., Stewart, C., Sword-Daniels, V., 2011. Volcanic ash impacts on critical infrastructure. Phys. Chem. Earth Pt. A/B/C.
Wright, H., Cashman, K., Rosi, M., Cioni, R., 2007. Breadcrust bombs as indicators of Vulcanian eruption dynamics at Guagua Pichincha volcano, Ecuador. Bull. Volcanol. 69, 281–300.
Zanella, E., Astis, G., Lanza, R., 2001. Palaeomagnetism of welded, pyroclastic-fall scoriae at Vulcano, Aeolian archipelago. J. Volcanol. Geotherm. Res. 107, 71–86.
Zuccaro, G., Cacace, F., Spence, R.J.S., Baxter, P.J., 2008. Impact of explosive eruption scenarios at Vesuvius. J. Volcanol. Geotherm. Res. 178, 416–453.